



HAL
open science

Bipolar “table with legs” resistive switching in epitaxial perovskite heterostructures

Sarunas Bagdzevicius, Michel Boudard, José Manuel Caicedo, Xavier Mescot, Raquel Rodriguez-Lamas, José Santiso, Mónica Burriel

► **To cite this version:**

Sarunas Bagdzevicius, Michel Boudard, José Manuel Caicedo, Xavier Mescot, Raquel Rodriguez-Lamas, et al.. Bipolar “table with legs” resistive switching in epitaxial perovskite heterostructures. *Solid State Ionics*, 2019, 334, pp.29-35. 10.1016/j.ssi.2019.01.027 . hal-02055426

HAL Id: hal-02055426

<https://hal.science/hal-02055426>

Submitted on 2 Apr 2020

HAL is a multi-disciplinary open access archive for the deposit and dissemination of scientific research documents, whether they are published or not. The documents may come from teaching and research institutions in France or abroad, or from public or private research centers.

L'archive ouverte pluridisciplinaire **HAL**, est destinée au dépôt et à la diffusion de documents scientifiques de niveau recherche, publiés ou non, émanant des établissements d'enseignement et de recherche français ou étrangers, des laboratoires publics ou privés.

Bipolar “table with legs” resistive switching in epitaxial perovskite heterostructures

Sarunas Bagdzevicius^{1*}, Michel Boudard^{1*}, José Manuel Caicedo², Xavier Mescot³, Raquel Rodríguez-Lamas^{1,2}, Jose Santiso² and Monica Burriel^{1*}

¹Univ. Grenoble Alpes, CNRS, Grenoble INP^{2*}, LMGP, F-38000 Grenoble, France

²Catalan Institute of Nanoscience and Nanotechnology (ICN2), CSIC and Barcelona Institute of Science and Technology (BIST), Campus UAB, Bellaterra, 08193 Barcelona, Spain

³Univ. Grenoble Alpes, Univ. Savoie Mont Blanc, CNRS, Grenoble INP^{2*}, IMEP-LAHC, F-38000 Grenoble, France

Abstract

We report the experimental investigation of bipolar resistive switching with “table with legs” shaped hysteresis switching loops in epitaxial perovskite $\text{GdBaCo}_2\text{O}_{5+\delta}/\text{LaNiO}_3$ bilayers deposited by pulsed laser deposition. The possibility of varying the resistivity of $\text{GdBaCo}_2\text{O}_{5+\delta}$ by changing its oxygen content allowed engineering this perovskite heterostructure with controlled interfaces creating two symmetric junctions. It has been proved that the resistance state of the device can be reproducibly varied by both continuous voltage sweeps and by electrical pulses. The symmetric devices show slightly non-symmetric resistance profiles, which can be explained by a valence change resistive switching model, and presented promising multilevel properties required for novel memories and neuromorphic computing.

Keywords: resistive switching, perovskite memristors, interface-type switching, ReRAM, multilevel ReRAM, valence change mechanism

^{1*}Corresponding authors: Sarunas Bagdzevicius, Michel Boudard and Monica Burriel;

E-mail address: sarunas.bagdzevicius@gmail.com, michel.boudard@grenoble-inp.fr, monica.burriel@grenoble-inp.fr;

Address: Minatec 3, Parvis Louis Néel CS 50257, 38016 GRENOBLE Cedex 1 France;

Phone: +33 (0) 4 56 52 93 43, fax: +33 (0) 4 56 52 93 01.

^{2*}Institute of Engineering Univ. Grenoble Alpes

Introduction

During the last 15 years, there has been a huge interest in the development of memristive devices (resistive switching memories) both in the industry and in academia. The first targeted application of these devices has been its use as non-volatile memory (NVM), in particular, the so-called redox-based resistive switching random access memory (ReRAM). ReRAMs are currently considered as one of the most promising emerging NVMs, in particular for embedded memory applications and as future storage class memory. The most remarkable properties of ReRAMs include fast writing speed, low energy consumption, high endurance, long retention times and good scalability[1]. Secondly, memristive devices can also be used for neuromorphic (brain-inspired) computing, where they offer enormous advantages due to the facility of connecting them in a simple crossbar array geometry and due to their small scalable size[2]. For logic applications the device requirements include the possibility of obtaining multilevel resistance states, good reliability, a large window of operation (ON/OFF ratio), a linear change in resistance upon set and reset as well as the possibility of mimicking brain functions, such as synaptic plasticity and learning, through engineered circuits constructed with ReRAMs[2].

While the best-performing ReRAMs are based on binary oxides (such as Ta_2O_5 , TiO_2 or HfO_2) and rely on filamentary-type switching (creation/rupture of oxygen vacancy filaments), some limitations such as reliability, cell-to-cell and cycle-to-cycle variability and noise issues, should still be overcome. These drawbacks are largely related to the stochastic nature of the filament formation. On the other hand, transition metal oxides (TMOs) based on interfacial or volume-type resistive switching (RS) seem to be a promising alternative for memristors, to better control the switching and to obtain multilevel analogue states[3]. The interest of studying TMOs, and in particular perovskite oxides, is that for many compounds it is possible to control the resistivity of the material by changing its oxygen vacancy content, concomitant to a change in the oxidation state of the transition metal oxide.

The switching properties of a memristive cell are highly dependent on the materials and dimensions of each element of the device (typically top and bottom electrodes and active switching material), as well as on the electrical signals applied to the system. In most cases, two electrodes of different nature are used to build a metal-insulator-metal type device. However it has been demonstrated that it is also possible to obtain resistive switching for a number of perovskite-based devices which are symmetrical: single devices with 2 symmetrical interfaces for PLCMO ($\text{Pr}_y\text{La}_{0.375-y}\text{Ca}_{0.325}\text{MnO}_3$) and YBCO ($\text{YBa}_2\text{Cu}_3\text{O}_7$) bulk polycrystalline samples[4]; PCMO ($\text{Pr}_{0.7}\text{Ca}_{0.3}\text{MnO}_3$) epitaxial thin films grown on LaAlO_3 substrate with Ag electrodes[5,6]; and PCMO layers grown on a YBCO bottom electrode (on top of a LAO substrate) with top Ag electrodes [6]. In the latter case, a symmetric device was obtained by measuring two Ag/PCMO/YBCO, YBCO/PCMO/Ag memristors in a back-to-back configuration. In all the above-mentioned cases the

resistive switching mechanism is mainly interface-type and results in a “table with legs” type switching. This name refers to the shape of the symmetric device resistance vs voltage hysteresis curve, which is very different from the usual rectangular hysteresis switching loop (HSL)[5]. This particular shape was properly described by symmetric device modeling and results from the superimposition of 2 devices with the usual rectangular-shape HSL switching in opposite direction[6]. In a later work Rozenberg *et al.* demonstrated by numerical simulations how by inducing asymmetry into the system the obtained “table with legs” hysteresis curve gradually evolves towards a conventional rectangular HSL cycle[4].

In this work we have selected a new perovskite material, namely GBCO ($\text{GdBaCo}_2\text{O}_{5+\delta}$), to construct a symmetric memristive devices in a back-to-back configuration. GBCO was selected due to its rich phase diagram and the possibility of tuning its electrical properties by changing its cation or oxygen stoichiometry. In particular, starting with the stoichiometric $\text{GdBaCo}_2\text{O}_{5.5}$ parent compound (insulator) the material can be continuously doped by either electrons or holes[7]. At room temperature, by increasing the oxygen content it changes from paramagnetic insulator to paramagnetic metal. In addition, a metal-insulator (MI) transition occurs slightly above room temperature ($T \approx 360$ K), which occurs gradual or sharper depending on the oxygen content of GBCO[7]. In addition, for epitaxial GBCO films grown by pulsed laser deposition (PLD) the electronic conductivity was shown to depend on the cationic composition (eg. (Gd+Ba)/Co ratio) and the presence of stacking defects (supplementary GdO planes along the *c*-axis of the material) resulted in a decrease in conductivity[8]. Furthermore, the strain induced by the epitaxial growth also seemed to contribute to the broadening of the MI transition temperature[8].

Due to its high oxygen diffusion properties, GBCO has been studied as alternative cathode material for solid oxide fuel cells [9]. Polycrystalline $\text{GdBaCo}_2\text{O}_{5.5+\delta}$ has a layered (double perovskite) structure, in which Gd and Ba are ordered in alternating (001) layers, with orthorhombic Pmmm space group and lattice parameters of $a = 0.3881(1)$ nm, $b = 0.7840(2)$ nm and $c = 0.7563(2)$ nm [10]. High oxygen diffusion coefficients were measured at intermediate temperatures (300-500 °C) both in the bulk form [10] and for epitaxial GBCO thin films[11]. In the latter case, it was proved that the oxygen diffusion depends on orientation, being about one order of magnitude lower along the *c*-axis of the structure. The possibility of tuning the electronic properties, together with the high oxygen diffusivity of the material motivated our interest to study of GBCO as novel memristive oxide.

In this article, we report on the RS properties of a symmetric device of two Ag/GBCO/LaNiO₃ LaNiO₃/GBCO/Ag memristors constructed in back-to-back configuration for the first time. We show how this symmetric device configuration presents “table with legs” type RS and multilevel resistance states. The devices have been measured by performing pulsed electrical measurements and current-voltage sweeps. We have also studied the conduction mechanisms for the different resistance states. Finally, a qualitative

model is presented explaining how the oxygen vacancy drift resulting from the applied voltage could change the resistance of the device resulting in the memristive properties presented.

Materials and methods

GdBaCo₂O_{5+δ} (GBCO) / LaNiO₃ (LNO) bilayers were deposited by PLD from ceramic targets using a KrF excimer laser (248 nm wavelength). In the case of GBCO a target with 5% wt. excess of Co was used to compensate for the volatility of the element. The heterostructures were constructed using a bottom LNO layer (28-61 nm thickness) as electrode, on top of which a film of GBCO (10-37 nm thickness) was grown. The following deposition parameters were used for the deposition of both perovskite oxides: laser fluence 1.1 J/cm², pulse repetition rate 10 Hz, substrate temperature 700 °C, oxygen partial pressure 60 mTorr.

The films were measured by XRD (X-ray diffraction) with a high-resolution diffractometer (D8 Discover, Bruker, Germany) using a monochromatic Cu_{K_α} source. The XRD pattern (Fig. 1a) shows an epitaxial (cube on cube) growth of the GBCO and LNO layers on top of SrTiO₃ (STO) substrates, as only 00l Bragg peaks with integer l values (using a pseudocubic cell indexing scheme) for the two perovskites are observed. The high-resolution XRD enlarged area close to STO 002 Bragg peak (Fig. 1b) shows the Bragg peaks of both layers, from which the experimental out-of-plane lattice parameters can be calculated and correspond to 0.3837 nm for GBCO and 0.3869 nm for LNO. The calculated pseudocubic lattice parameter for the LNO layer ($a_{\text{out-of-plane}} = 0.3869$ nm) is only slightly larger than that of bulk LNO [12] $a_{\text{pc}} = 0.386$ nm. The high coherence and quality of the epitaxial films, together with low roughness and smooth interphase are confirmed by the observed Kissing fringes, from which the thickness of the LNO layer was calculated (27.5 nm for this particular film) and by the TEM images shown below (Fig. 2).

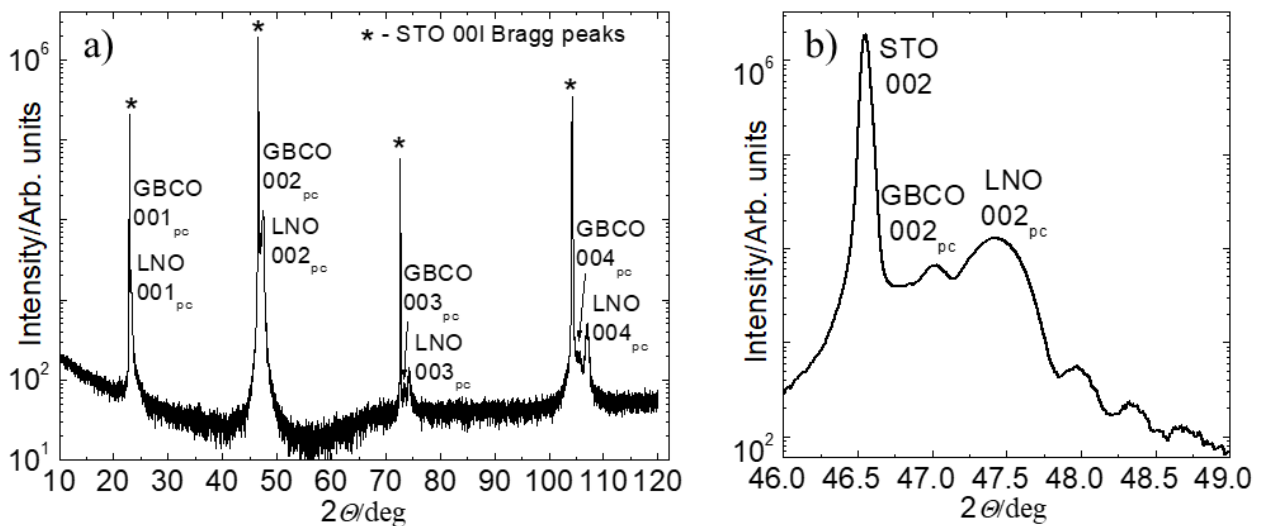


Fig. 1. XRD pattern of the GBCO/LNO//STO heterostructure. a) Epitaxial GBCO and LNO layers in which only the 00l Bragg peaks ($l = \text{integer}$, pseudocubic cell) are observed. b) The enlarged area close to STO 002 Bragg peak (Kissing fringes corresponds to the LNO layer thickness of 27.5 nm). $\text{GdBaCo}_2\text{O}_{5+\delta}$ = GBCO, LaNiO_3 = LNO and SrTiO_3 = STO.

Scanning Transmission Electron Microscopy (STEM) image (Fig. 2c) shows that the bilayer is formed by highly dense and flat films with a well-defined interface. The LNO layer thickness calculated from the XRD data perfectly coincides with the layer thickness measured by the STEM. The HRTEM image (Fig. 2a) indicates that the GBCO film is composed by a mixture of single and double perovskite domains, with the c -axis oriented both in-plane and out-of-plane. Accordingly, the selected area electron diffraction pattern (SAED) of the heterostructure (Fig. 2b) shows the diffraction peaks corresponding to a double perovskite lattice of GBCO (superlattice peaks) in two perpendicular directions with a cube on cube epitaxial relationship (the powder ring pattern observed in SAED at low angles comes from the sample preparation). The existence of defects (dislocations [13] and stacking faults [14]) in the LNO film, which could have been formed at the growth temperature and/or during the cooling down to room temperature after the deposition, are observed in the TEM images as shown in Fig. 2a. In the LNO layer defects with an out-of-plane oriented stripe contrast can be observed in Fig 2a and correspond to $(0k0)$ oriented streaks in the selected area electron diffraction (SAED), as shown in Fig. 2b.

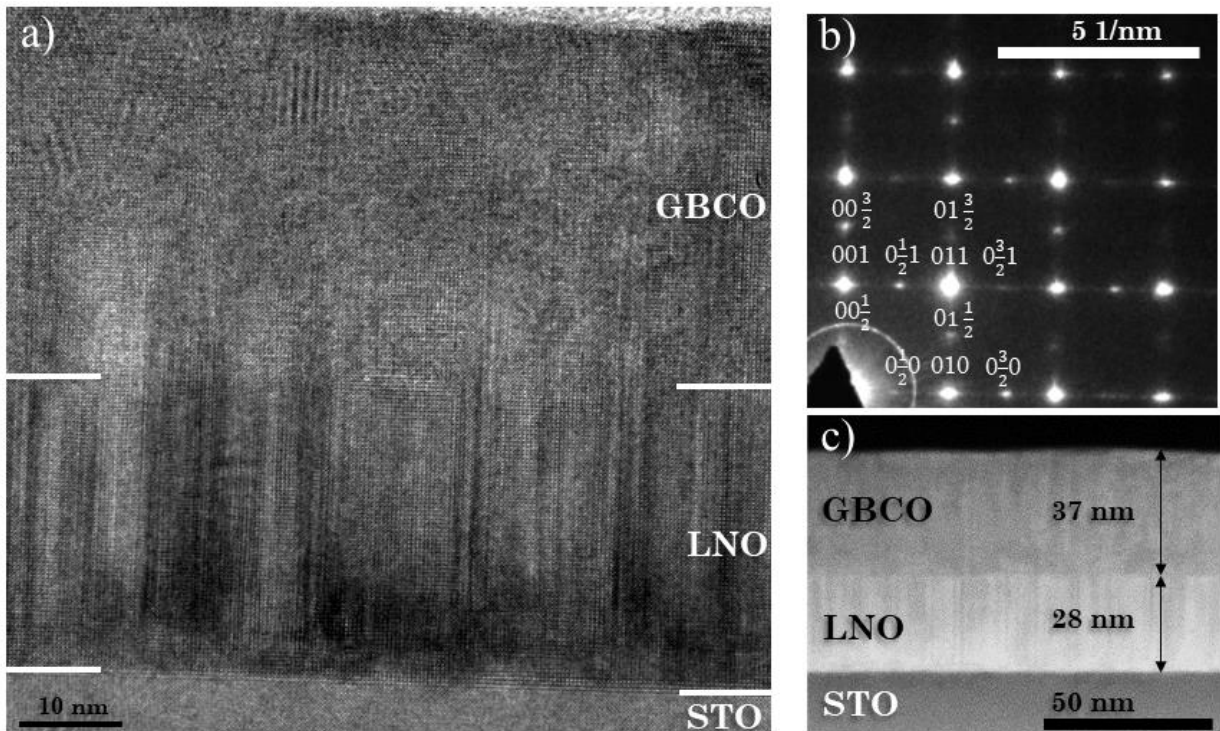


Fig. 2. HRTEM cross-section a) of the GBCO/LNO//STO heterostructure. b) Selected area electron diffraction pattern (SAED) of the heterostructure; the diffraction peaks correspond to a double perovskite lattice of GBCO (superlattice peaks) with a cube on cube epitaxial relationship. c) STEM HAADF Z-contrast image (80 mm camera length) of the heterostructure. $\text{GdBaCo}_2\text{O}_{5+\delta}$ = GBCO, LaNiO_3 = LNO and SrTiO_3 = STO.

The GBCO layer grows epitaxially following the LNO template, with some defects extending from LNO into the GBCO layer, as shown in Fig. 2a and c. Within the GBCO layer, there are some regions that show a clear double-layered structure (double periodicity) along either the vertical or horizontal direction. However, the largest part of GBCO shows a perfect single perovskite structure. Nevertheless, a clear evidence of the GBCO lattice doubling can be observed by the appearance of the superlattice peaks in the SAED pattern (Fig. 2b). The diffraction peaks were indexed in the symmetry space of the GBCO orthorhombic double perovskite.

Prior to RS investigation in GBCO/LNO bilayers, the electrical properties of individual GBCO and LNO single layers were probed obtaining resistivity values of ρ (LNO) = 120 - 170 $\mu\Omega\cdot\text{cm}$ and ρ (GBCO) = 95 $\text{m}\Omega\cdot\text{cm}$ at room temperature. As shown in Fig. 3a, the circle-shaped silver top electrodes (50 to 200 μm diameter circles, 100-200 μm apart) were e-beam evaporated on top of the bilayer heterostructures after a gentle Ar plasma cleaning. Depending on the sample, the device geometry was defined either by UV laser-lithography or by the use of a shadow mask. The final symmetric device in which the electrical characterization was carried out comprises two active junctions in the back-to-back configuration: Ag/GBCO/LNO and LNO/GBCO/Ag as shown in Fig 3a. DC electrical characterization was carried out at ambient conditions within a Faraday cage with microprobe manipulators and using an Agilent B1500 semiconductor parameter analyzer with triaxial cables for low current measurements. As ReRAMs typically work with pulsed voltages both integrated or in the standalone form, we have characterized the devices and induced RS, by applying pulses, in addition to by $I(V)$ sweeps. Furthermore, the pulsed measuring mode avoids the main drawback of the $I(V)$ sweeps, such as transient regimes.

Results and discussion

Electrically induced resistive switching (RS) was investigated by a two-point measurement method in a symmetric device consisting of two active junctions in a back-to-back configuration (Ag/GBCO/LNO and LNO/GBCO/Ag). The protocol used for measuring the HSL is shown in Fig. 3b. Increasing voltage pulses of approx. 2 s duration were used to write (change the state of the device) and 40 ms / -50 mV pulses were used to read (measure the state).

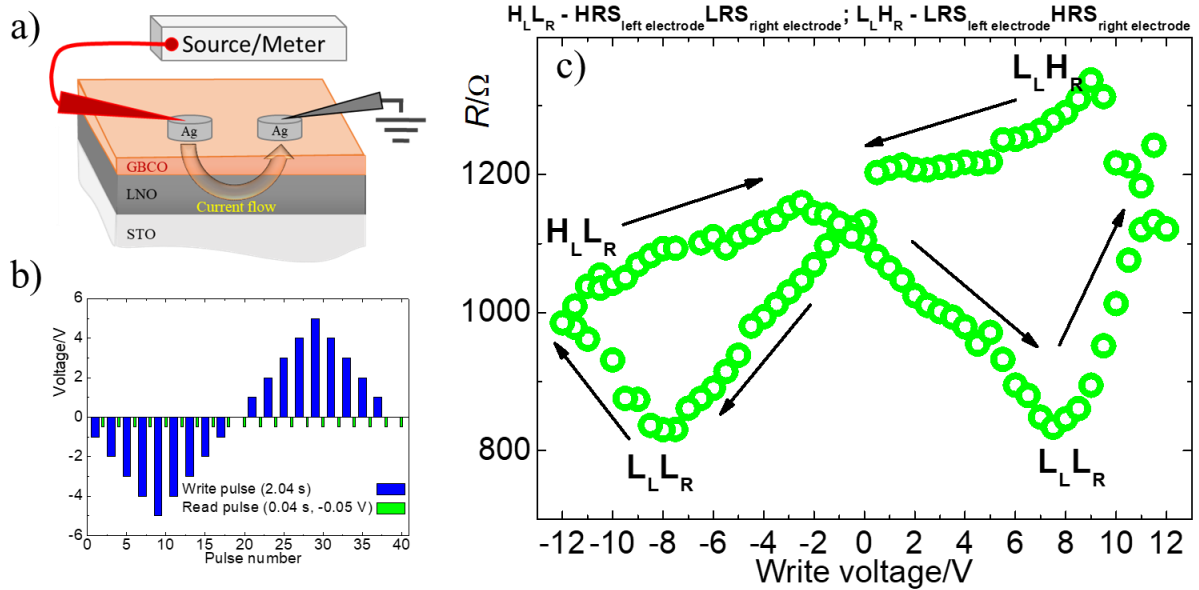


Figure 3. “Table with legs” HSL measured in pulsed voltage mode. a) Sketch of the devices (not to scale) used for the electrical measurements. GBCO thickness from 10 to 37 nm, LNO thickness from 28 to 61 nm. Top Ag electrodes: 100 nm thickness, 50 – 200 μm diameter and 100 - 200 μm distance between two electrodes. b) Pulse measurement scheme. c) “Table with legs” HSL for remnant resistance measured with read pulses at -50 mV after each write pulse with the following Ag electrodes geometry: 50 μm diameter and 100 μm separation; and 10/61 nm GBCO/LNO thicknesses ($H_L L_R$ – $HRS_{\text{left pad}} LRS_{\text{right pad}}$; $L_L H_R$ – $LRS_{\text{left pad}} HRS_{\text{right pad}}$; $L_L L_R$ – $LRS_{\text{left and right pads}}$).

RS was induced for the GBCO/LNO heterostructures in both junctions during the same voltage cycle. During the HSL in pulse mode, one active junction switches to the low resistance state (or LRS, hereafter L_R and L_L corresponding to the left and right junctions, respectively) and the other one to the high resistance state (or HRS, hereafter H_R and H_L corresponding to the left and right junctions, respectively), but these processes occur at different voltages. The resistance change (Fig. 3c) shows a “table with legs” shape HSL which switches in *eight-wise* direction starting by the application of negative voltage pulses. In our case, the electrical potential is always applied to the left junction, coinciding with the geometrical left side in Fig. 3a.

At the beginning of the electrical characterization the device (both junctions) are in an undetermined state. After a few $I(V)$ sweeps or pulse cycles the device initializes and reaches the steady mode with one junction being in H and the other one in L state (as shown in Figs. 4 and 5). When applying increasing pulses from 0 V to -12 V, and back to 0 V first and from 0 V to +12 V, to 0 V after (protocol shown in Fig. 3b and one full pulse cycle in Fig. 3c) the following switching occurs: When applying consecutive negative pulses from 0 V to -8 V the left electrode is kept in L_L . On the other hand, the right electrode junction

changes from its H_R (close to 0 V) to the L_R , and the device reaches the lowest resistance state ($L_L L_R$) at -8 V (Fig. 3c). When further decreasing the negative bias from -8 V to -12 V, the left electrode junction switches from L_L to H_L and, as a result, the overall resistance increases (Fig. 3c, $H_L L_R$ at -12 V). A symmetric switching sequence was observed when positive voltage pulses were applied cycling from 0 V to +12 V and back to 0V : the right electrode is kept in L_R while the left electrode junction goes from H_L close to 0 V to the L_L close to +8 V ($L_L L_R$ at 8 V in Fig. 3c). Finally, by increasing the positive voltage (above 8 V) the right electrode junction switched to the H_R and the memristive device's resistance returned to its initial value ($L_L H_R$ state, approx. 1200 Ω close to 0 V in Fig. 3c). The resistance state of each junction (left and right) was determined by the resistance measurement (non-switching, at low voltage) using a third electrode. The reference electrodes were Ag electrodes of the same size, deposited on top of the GBCO film and equidistantly located from the two probed ones. All changes in resistance (L to H and H to L) were gradual occurring over a voltage interval, in agreement with interface or volume-type switching mechanisms (non-filamentary). There is 300 Ω difference between $H_L L_R$ and $L_L H_R$ (Fig. 3c) which can be explained by different H resistance values due to the small deviations in the initial resistance conditions (first non-switching cycles as in Fig. 5a). By cycling, small initial resistance differences are subsequently enhanced for the junction in which there is a larger voltage drop.

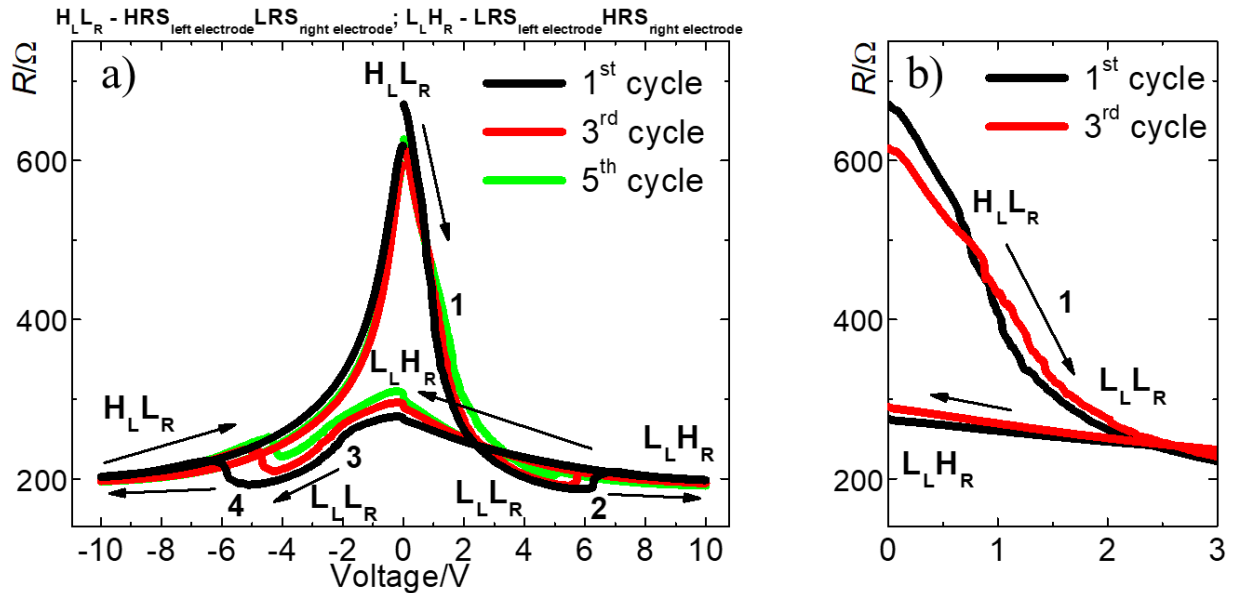


Fig. 4. RS measured on a symmetric device built by two Ag/GBCO/LNO and LNO/GBCO/Ag junctions in series (voltage sweep mode). Instantaneous resistance during voltage sweep with the following Ag electrodes geometry: 200 μm diameter and 200 μm separation; and 37/28 nm GBCO/ LNO thicknesses. The four switching events are marked in the graph with numbers 1 to 4. a) Two junctions in series reproducibly switched between $H_L L_R$ and $L_L H_R$ resistance states by $I(V)$ cycling and b) zoom-in of the 0 to

+3V voltage range, where the characteristic small R drops related to multiple transitions are observed ($H_L L_R - HRS_{\text{left electrode}} LRS_{\text{right electrode}}, L_L H_R - LRS_{\text{left electrode}} HRS_{\text{right electrode}}$).

As shown in Figures 4 and 5, the resistance-voltage (R–V) curves in sweep mode for the two back-to-back junctions (situated 100 and 200 μm apart) measured in series are continuous and reproducible and present a characteristic “sombbrero” symmetrical shape. *Chen et al.* [15] observed a similar, but asymmetric, shape for the resistance-sweep curves of a single $\text{SiO}_2\text{:Pt}$ RRAM and explained the curves by a generalized multipath switching model. They relate the on-switching spread over several volts with multiple transitions involving a multitude of intermediate-resistance-states (IRS), which correspond to in series parallel switchable elements in the film. In Fig 4b, by zooming-in the low voltage positive range, the characteristic small R drops related to multiple transitions are featured for our GBCO-based symmetrical devices (point 1). As our system is composed by two mirrored devices, in this case the total $R(V)$ curve will correspond to the superposition of 2 mirrored asymmetric $R(V)$ curves, resulting in the observed symmetric sweep “sombbrero” shaped curves.

In Fig. 4a a highly non-linear conduction appears for $|V| < 2\text{V}$. The observed *clockwise* R-V switching is double, which means that for the same half-cycle switching events occur in two different junctions in series; while one junction switches to the L other switches to H. The four switching events taking place for each complete R-V cycle (positive and negative voltage) are marked in Fig. 4 with numbers 1 to 4. The switching occurs in the following way: the highest resistance ($R \approx 650 \Omega$) corresponds to the initial resistance state ($H_L L_R$ close to 0V in Fig. 4a). By increasing the positive electric potential (with respect to the left Ag electrode) the left junction switches to L_L close to +2V (Fig. 4a point 1). Between point 1 and point 2 (Fig. 4a) both the left and the right junctions are in L state, thus showing the smallest overall resistance ($R < 200 \Omega$). When the positive bias surpasses +6V the right junction switches from L_R to H_R , and then the GBCO-based device is in $L_L H_R$ state, state which is withheld while decreasing the positive potential. Due to the asymmetry in the electrical potential distribution in the device, two junctions in series act as a voltage divider and the voltage drops differerently depending on the initial resistance of each junction. As a result the $L_L H_R$ state close to 0V bias shows smaller overall resistance ($R \approx 300 \Omega$) than the $H_L L_R$ state ($R \approx 600 \Omega$). When the negative potential reaches -3V (Fig. 4a point 3), the right junction switches to L_R and the device reaches another $L_L L_R$ state (at a negative bias, between points 3 and 4 in Fig. 4a). By further increasing the negative voltage down to almost -6 V (at point 4 in Fig. 4) the left junction switches to the H_L and the device state comes back to the initial $H_L L_R$.

In Fig. 5a we can observe how the hysteresis in the R-V curves developed gradually when increasing the cycling voltage range, in this case for two junctions which are 100 μm apart. No RS hysteresis effect was observed when the sweeping voltage was kept below $|V_{max}| = 5\text{V}$ (not shown in Fig 5a). A small

opening (non-reproducible) appeared at $|V_{max}| = 5V$ (0V, +5V, 0V, -5V and 0V cycle) (red line in Fig 5a) and, finally, the hysteresis becomes stable showing the presence of the two equivalent mirrored components ("sombbrero" shaped curve) for $|V_{max}|$ larger than 5V (green and blue lines in Fig 5a). The device started switching when cycling above $|V_{max}| = 5V$ (Fig. 5a), finally developing a reproducible resistive switching behavior (two distinguishable $H_L L_R$ or $L_L H_R$ states and two $L_L L_R$ or $L_L H_R$ states for positive and negative voltage in Fig. 5a respectively).

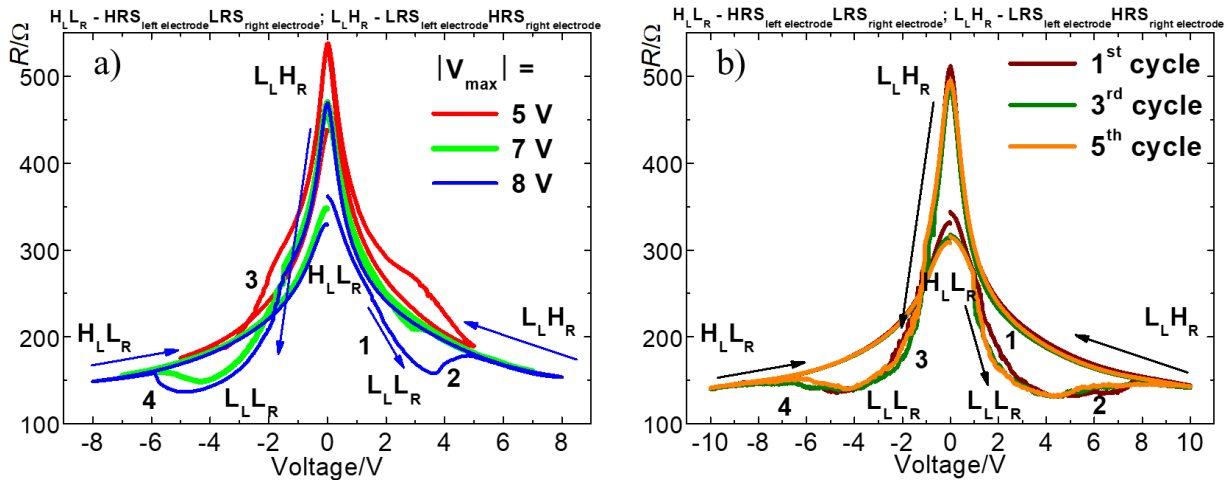


Fig. 5. Instantaneous resistance during $I(V)$ sweeps. a) RS hysteresis development with the increase of the maximum voltage applied in each cycle. RS hysteresis increases on the increase of the voltage range in a) and develops into reproducible switching in b) when increasing the number of cycles. b) The device is reproducibly switched between $H_L L_R$ and $L_L H_R$ resistance states by $I(V)$ sweeps when cycled between -8 and 8 V. ($H_L L_R - HRS_{\text{left electrode}} LRS_{\text{right electrode}}$, $L_L H_R - LRS_{\text{left electrode}} HRS_{\text{right electrode}}$). Ag electrodes geometry: 200 μm diameter and 100 μm distance apart, 37/28 nm GBCO/LNO thicknesses.

When measuring different pairs of devices in back-to-back configuration it was not predetermined which one of the resistance states ($H_L L_R$ or $L_L H_R$) would have highest total resistance. In Fig. 5b we observe that the resistance of $L_L H_R$ is larger than that of $H_L L_R$, while the opposite is true for the devices presented in Fig. 4. Nevertheless, it is important to note that there was always a clear resistance difference between $H_L L_R$ and $L_L H_R$ in our devices. The main differences in the $R(V)$ curve comparing with the device shown in Fig. 4a is that the resistance value for the $H_L L_R$ in Fig 5b (close to 0 V bias,) is lower than that of the $L_L H_R$ and less asymmetric $L_L L_R$ states are observed ($L_L L_R$ in the positive bias side in Fig. 4 and $L_L L_R$ in the negative bias side in Fig. 4). We would like to note that the $R(V)$ curves as shown in Fig. 4a and Fig. 5a become more symmetric as the voltage range increases. In addition, the overall device resistance value (measured close to 0 V) shows area scaling. The devices with smaller top Ag electrode (50 μm pad diameter, $L_L H_R$

with approx. 1200Ω) showed higher resistance than the larger Ag electrode devices ($200\ \mu\text{m}$ pad diameter, $H_L L_R$ with approx. 600Ω) in agreement with the geometrical resistance.

To better illustrate the area-scaling, RS has been measured in $I(V)$ sweep mode for the same sample using Ag electrode pads of different size; the results are shown in Fig 6. The resistance values have been extracted for $L_L L_R$ at the resistance minima (both for negative and positive voltages), corresponding to 2 V below the switching threshold; and at -10 V and +10 V for the $H_L L_R$ and $L_L H_R$ states, respectively. The area-scaling of the different resistance states is clearly shown in Fig 6b. These observations are in good agreement with an interface or volume-type resistance switching mechanism active in the GBCO/LNO junctions (non-filamentary type RS).

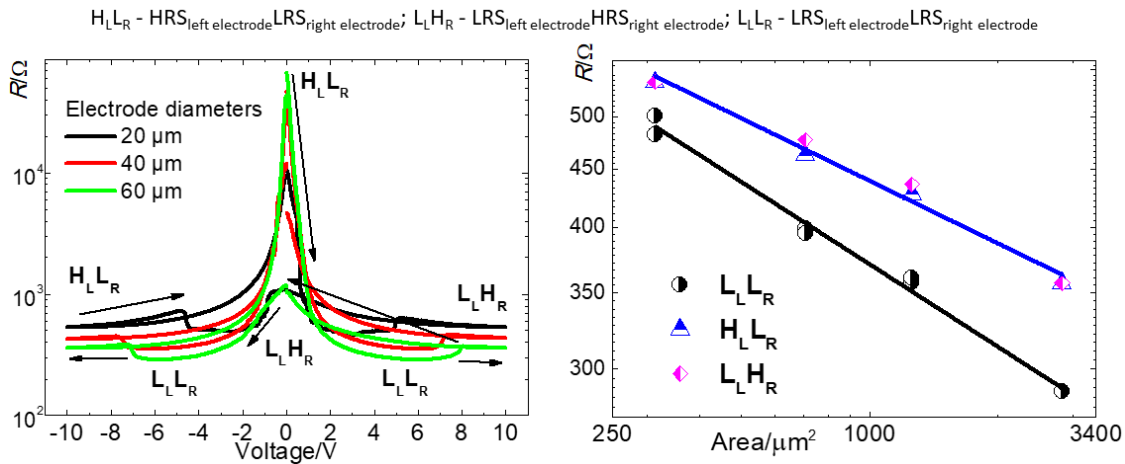


Fig. 6. Area-scaling. $I(V)$ plots in a) of the symmetric device's Ag electrode pads of three different sizes (20-60 μm diameter, 100 μm apart). Resistances in b) of two LRS states in series ($L_L L_R$, black circles) measured 2 V below the switching voltage both in positive and negative polarity, $H_L L_L$ measured at -10 V (blue triangles) and $L_L H_R$ measured at 10 V (pink diamonds), lines are linear fits.

Plotting the $I(V)$ curves corresponding to Fig. 4a and 5b in log-log representation allows obtaining preliminary insight into the conduction mechanisms through the active heterostructure when the device is switched to the different resistance states, as almost all considerable conduction mechanisms in the oxides have an exponential and/or power law term in the $I(V)$. For further details into the conduction mechanisms' equations the reader is referred to ref.[16]. At low voltages (below 0.5V, see Fig. 7a and 7b) and in both $H_L L_R$ and $L_L H_R$ resistance states, the conduction mechanism is clearly linear and dominated by ohmic conduction with the exponent close to 1. When the device switches to the $L_L L_R$ state, at the intermediate voltage range (e.g. from 1 to 6 V for the positive voltage in Fig. 7a) the mechanism is no longer linear (non-ohmic) with exponent around 1.33-1.35 (Fig. 7a and 7b). At the highest voltages (close to 10V) and $H_L L_R$ or $L_L H_R$ the conduction becomes again ohmic. Looking more in detail, the almost ohmic conduction for the

$L_L H_R$ (and $H_L L_R$) state in Figs. 7a and 4 (and Figs. 7b and 5 b, respectively) extends over a larger voltage range than that of the $H_L L_R$ (and $L_L H_R$) state. This observation gives the indication that mainly the L state (lowest resistance state when combining left and right junctions resistances) is responsible of the ohmic conduction and has been further analysed next by using the gamma γ ($= d \ln I / d \ln V$) analysis (see details in references [16-17]).

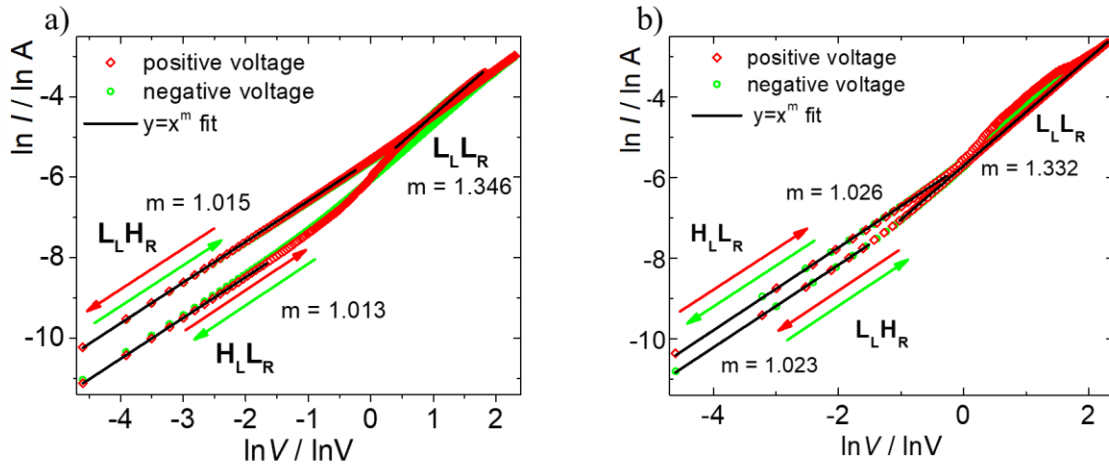


Fig. 7. $I(V)$ curves in logarithmic scale corresponding to figures 4a and 5b. At low voltage both for positive (red diamonds) and negative bias (green circles) the conduction mechanism is ohmic. At the intermediate voltage range ($L_L L_R$ states) the conduction mechanism shows a deviation from ohms law.

Figure 8 shows the γ analysis of the $I(V)$ curve shown in Fig. 4a at room temperature. They have been calculated for the $H_L L_R$ resistance state from third cycle (red curve in Fig. 4) in the negative voltage region (increasing voltage from -10 V to 0 V) and the $L_L H_R$ state in the positive voltage region (decreasing voltage from 10 V to 0 V in Fig. 4a), regions in which no transitions are observed and thus are expected to be close to the characteristic curve measured in steady regime without hysteresis. The $L_L H_R$ (red curve in Fig 8) is dominated by an ohmic component corresponding to a constant γ value of 1. A small overimposed component corresponding to a linear dependence of γ against $V^{1/2}$ (characteristic of Poole-Frenkel and Schottky conduction mechanisms) is observed up to 6 V in voltage (sqrt $V^{1/2}$ reaching almost 2.5). A similar, but much larger component (larger slope) dominates the conduction mechanism at low voltage for the $H_L L_R$ state (black curve in Fig 8) up to 1 volt. The inset of figure 8 shows $I(V)$ representation for the low voltage region. Whereas the $H_L L_R$ state (black curve) presents non-linear behaviour, the $L_L H_R$ (red curve) is almost ohmic, in good agreement with the γ analysis.

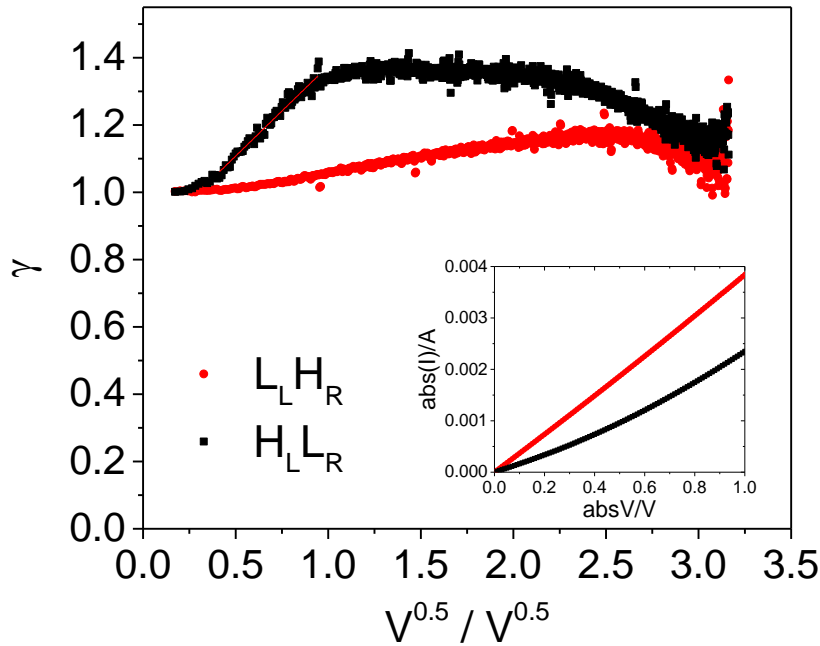


Fig. 8. γ as a function of $V^{1/2}$, corresponding to the $H_L L_R$ state (red circles) and the $L_L H_R$ (black squares) in figure 4a. The inset shows $I(V)$ at low voltages showing a close-to-ohmic ($L_L H_R$) and non-linear ($H_L L_R$) dependence.

These preliminary results are compatible with an almost ohmic L states whereas the H states are highly non linear. The $H_L L_R$ is clearly dominated by the H component, whereas this component is much less important in $L_L H_R$ (a factor 2.4 lower evaluated from the resistance ratios measured in Fig. 4a). This explains the asymmetric behaviour of the device. The difference between the $H_L L_R$ and $L_L H_R$ states also explains the difference between figures 4 and 5, which shape, as previously described, is determined by the initial state of each junction, and can be tuned by changing the “initializing” or “forming” process (see details in reference [4]).

The observed “table with legs” resistive switching behaviour (Fig. 3c) when measuring using the pulsed voltage and the observed “sombbrero” shape for the $I-V$ sweep curves (Fig. 4 and 5) can be explained taking into account the movement of the charged species. In the literature it has been widely reported that for valence change type resistive switching (VCM), the change in resistance is provoked by the movement of oxygen vacancies, V_O^\bullet [1]. For GBCO, the presence of oxygen vacancies at the close proximity of the junctions would result in the observed resistance change [7] due to the created conduction barriers: Schottky barrier at the interface [18] or Poole-Frenkel barrier zone at the close proximity of the interface [19].

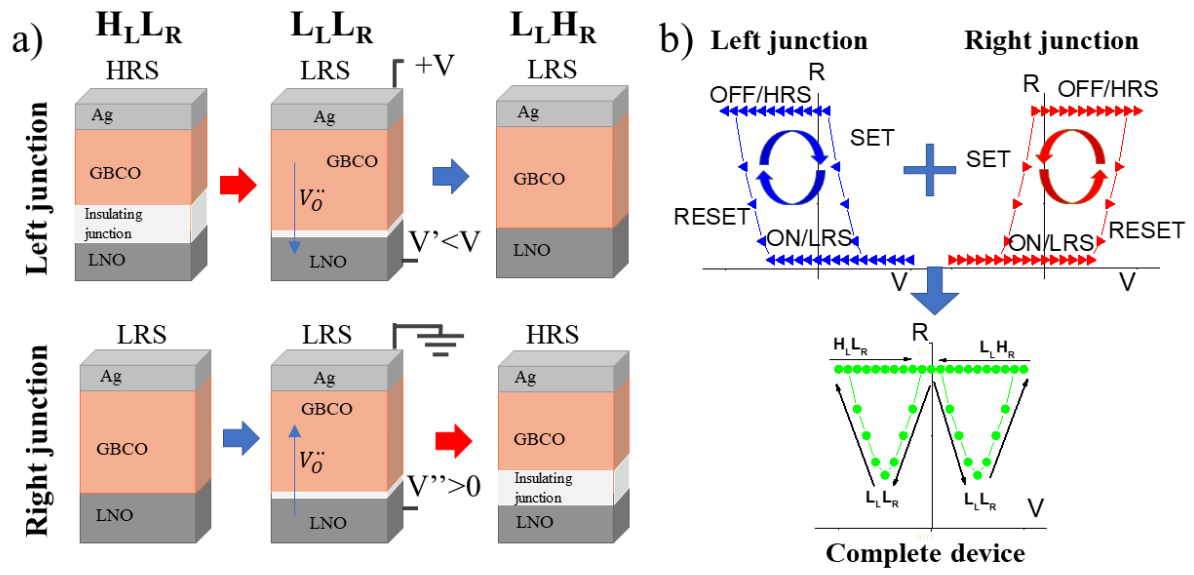


Fig. 9. Illustration of “table with legs” resistive switching. a) Scheme of the oxygen vacancies movement and interface resistance changes for positive voltage cycling (corresponding to Fig 3c and 5). Red and blue arrows indicate when a switching event occurs (with the voltage bias polarity as shown for the individual junctions in the device). b) Resistance change for each individual junction (left and right) and for the complete device in back-to-back configuration ($H_L L_R - HRS_{\text{left electrode}} LRS_{\text{right electrode}}, L_L H_R - LRS_{\text{left electrode}} HRS_{\text{right electrode}}, L_L L_R - LRS_{\text{left electrode}} LRS_{\text{right electrode}}$).

According to the switching dependence on the external bias polarity, we propose a simple model (see Fig. 9) explaining how the changes in resistance can be related to the oxygen vacancies movement induced by the electrical field, together with the creation/annihilation of an insulating interface (between GBCO and LNO). After a full $I(V)$ sweep or pulse cycle (0 V to $|10|$ V) the GBCO-based device initializes, reaching either the $H_L L_R$ (or $L_L H_R$) resistance state. As schematically illustrated in the Fig. 9a, when applying either positive or negative voltage above the L to H threshold (in our devices this reset threshold was between 6 and 8 V) the device switched from $H_L L_R$ to $L_L H_R$ (or vice versa, depending on the initial state). Before completely reversing the junctions states (from $H_L L_R$ to $L_L H_R$), both junctions are brought to the L ($L_L L_R$, central part of Fig. 9a), resulting in the “legs” of the typical observed $R(V)$ “table with legs” curve. The valence change mechanism (oxygen vacancies movement) hypothesis is reinforced by the “table with legs” shape of the $R(V)$ (schematically depicted in the Fig. 9b), which can be constructed by the superposition of the two independent $R(V)$ s of the separate switching junctions (Fig. 9b).

Conclusions

We have engineered epitaxial perovskite oxide GBCO/LNO bilayers, which showed RS in the $I(V)$ sweep and pulse modes at room temperature. The devices are composed of two switching junctions in back-to-back configuration and showed $R(V)$ curves with the so-called “table with legs” shape when measured using pulsed voltage and a “sombbrero” shape when measured using voltage sweeps.

The area scaling and the continuous $R(V)$ curves observed, with no sharp jumps for the transitions between resistance states, allows concluding that our devices possess interface or volume type RS (non-filamentary).

Finally, we have shown that the RS of the GBCO-based devices shows gradual transitions, which could potentially allow to obtain multiple intermediate states, instead of only two different states, as is the typical case of filamentary-type RS. For these perovskite memristors, by using different electrical pulse sequences, it would be possible to obtain different resistance states covering, at least, the whole resistance range shown in the “table with legs” curves. The possibility of obtaining multiple levels of resistance in an “analogical” way is particularly interesting for applications such as neuromorphic computing.

Acknowledgments

Special acknowledgment goes to Goda Bagdzeviciute for fruitful discussions and moral support during the preparation of the manuscript.

Funding: This work has been financed by the ANR funded project “MICROSWITCH” (ANR-14-ACHN-0012) and by the “FUN-TO-BE” CNRS-CSIC supported International Program for Scientific Cooperation (PICS, n°PICS07294). In addition, this work has been performed with the help of the “Plateforme Technologique Amont” de Grenoble, with the financial support of the “Nanosciences aux limites de la Nanoélectronique” Foundation" and CNRS Renatech network and has benefited from the facilities and expertise of the OPE)N(RA characterization platform of FMNT (FR 2542, fmnt.fr) supported by CNRS, Grenoble INP and UGA.

Reference

- [1] D. Ielmini, R. Waser, Resistive switching: from fundamentals of nanoionic redox processes to memristive device applications, n.d.
- [2] D. Ielmini, Brain-inspired computing with resistive switching memory (RRAM): Devices, synapses

- and neural networks, *Microelectron. Eng.* 190 (2018) 44–53. doi:10.1016/j.mee.2018.01.009.
- [3] S. Bagdzevicius, K. Maas, M. Boudard, M. Burriel, Interface-type resistive switching in perovskite materials, *J. Electroceramics*. 39 (2017) 1–28. doi:10.1007/s10832-017-0087-9.
- [4] M.J. Rozenberg, M.J. Sánchez, R. Weht, C. Acha, F. Gomez-Marlasca, P. Levy, Mechanism for bipolar resistive switching in transition-metal oxides, *Phys. Rev. B*. 81 (2010) 115101. doi:10.1103/PhysRevB.81.115101.
- [5] X. Chen, N.J. Wu, J. Strozier, A. Ignatiev, Direct resistance profile for an electrical pulse induced resistance change device, *Appl. Phys. Lett.* 87 (2005) 1–3. doi:10.1063/1.2139843.
- [6] X. Chen, J. Strozier, N.J. Wu, A. Ignatiev, Y.B. Nian, A study of the symmetry properties and multi-state nature of perovskite oxide-based electrical pulse induced resistance-change devices, *New J. Phys.* 8 (2006) 229–229. doi:10.1088/1367-2630/8/10/229.
- [7] A.A. Taskin, A.N. Lavrov, Y. Ando, Transport and magnetic properties of $\text{GdBaCo}_2\text{O}_{5+x}$ single crystals: A cobalt oxide with square-lattice CoO_2 planes over a wide range of electron and hole doping, *Phys. Rev. B*. 71 (2005) 134414. doi:10.1103/PhysRevB.71.134414.
- [8] M. Burriel, M. Casas-Cabanas, J. Zapata, H. Tan, J. Verbeeck, C. Solís, J. Roqueta, S.J. Skinner, J. a. Kilner, G. Van Tendeloo, J. Santiso, Influence of the Microstructure on the High-Temperature Transport Properties of $\text{GdBaCo}_2\text{O}_{5+\delta}$ Epitaxial Films, *Chem. Mater.* 22 (2010) 5512–5520. doi:10.1021/cm101423z.
- [9] A. Tarancón, M. Burriel, J. Santiso, S.J. Skinner, J.A. Kilner, Advances in layered oxide cathodes for intermediate temperature solid oxide fuel cells, *J. Mater. Chem.* 20 (2010) 3799. doi:10.1039/b922430k.
- [10] A. Tarancón, S.J. Skinner, R.J. Chater, F. Hernández-Ramírez, J. a. Kilner, Layered perovskites as promising cathodes for intermediate temperature solid oxide fuel cells, *J. Mater. Chem.* 17 (2007) 3175. doi:10.1039/b704320a.
- [11] J. Zapata, M. Burriel, P. García, J.A. Kilner, J. Santiso, Anisotropic ^{18}O tracer diffusion in epitaxial films of $\text{GdBaCo}_2\text{O}_{5+\delta}$ cathode material with different orientations, *J. Mater. Chem. A*. 1 (2013) 7408. doi:10.1039/c3ta10749c.
- [12] J. Son, P. Moetakef, J.M. Lebeau, D. Ouellette, L. Balents, S.J. Allen, S. Stemmer, Low-dimensional Mott material: Transport in ultrathin epitaxial LaNiO_3 films, *Appl. Phys. Lett.* 96 (2010) 18–21. doi:10.1063/1.3309713.

- [13] L. López-Conesa, J.M. Rebled, D. Pesquera, N. Dix, F. Sánchez, G. Herranz, J. Fontcuberta, C. Magén, M.J. Casanove, S. Estradé, F. Peiró, Evidence of a minority monoclinic LaNiO_{2.5} phase in lanthanum nickelate thin films, *Phys. Chem. Chem. Phys.* 19 (2017) 9137–9142. doi:10.1039/C7CP00902J.
- [14] C. Coll, L. López-Conesa, J.M. Rebled, C. Magén, F. Sánchez, J. Fontcuberta, S. Estradé, F. Peiró, Simulation of STEM-HAADF Image Contrast of Ruddlesden–Popper Faulted LaNiO₃ Thin Films, *J. Phys. Chem. C*. 121 (2017) 9300–9304. doi:10.1021/acs.jpcc.6b12484.
- [15] A.B.K. Chen, B.J. Choi, X. Yang, I.-W. Chen, A Parallel Circuit Model for Multi-State Resistive-Switching Random Access Memory, *Adv. Funct. Mater.* 22 (2012) 546–554. doi:10.1002/adfm.201102208.
- [16] F.-C. Chiu, A Review on Conduction Mechanisms in Dielectric Films, *Adv. Mater. Sci. Eng.* 2014 (2014) 1–18. doi:10.1155/2014/578168.
- [17] C. Acha, A. Schulman, M. Boudard, K. Daoudi, T. Tsuchiya, Transport mechanism through metal-cobaltite interfaces, *Appl. Phys. Lett.* 109 (2016) 011603. doi:10.1063/1.4955204.
- [18] R.T. Tung, The physics and chemistry of the Schottky barrier height, *Appl. Phys. Rev.* 1 (2014). doi:10.1063/1.4858400.
- [19] J.G. Simmons, Poole-Frenkel Effect and Schottky Effect in Metal-Insulator-Metal Systems, *Phys. Rev.* 155 (1967) 657–660. doi:10.1103/PhysRev.155.657.